Strain engineering a persistent spin helix with infinite spin lifetime

Xue-Zeng Lu and James M. Rondinelli *
Department of Materials Science and Engineering, Northwestern University, Evanston, Illinois 60208, USA

(Received 24 August 2022; accepted 2 December 2022; published xxxxxxxxxx)

Persistent spin textures (PSTs) in solid-state materials arise from a unidirectional spin-orbit field in momentum space and offer a route to deliver long carrier spin lifetimes sought for future quantum microelectronic devices. Nonetheless, few three-dimensional materials are known to host PSTs owing to crystal symmetry and chemical requirements. There are even fewer examples demonstrated experimentally. Here we report that high-quality persistent spin textures can be obtained in the polar point groups containing an odd number of mirror operations. We use representation theory analysis and electronic structure calculations to formulate general discovery principles to identify PSTs hidden in known complex ternary layered and perovskite structures with large electric polarizations. We then show some of these materials exhibit PSTs without requiring any special crystalline symmetries. This finding removes the limitation imposed by mirror-symmetry protected PSTs that has limited compound discovery. Our general design approach enables the pursuit of persistent spin helices in materials exhibiting the C_{3v} crystal class adopted by many quantum materials exhibiting large Rashba coefficients.

DOI: 10.1103/PhysRevB.00.005100

I. INTRODUCTION

The persistent spin helix (PSH) is a spin-wave mode, in which the spin can propagate with an infinite spin lifetime [1–5]. This mode is enabled by a persistent spin texture (PST) in momentum space, whereby unidirectional spin-momentum locking occurs. This makes the PST a useful spin texture to protect against spin decoherence where it can be exploited in spin field-effect transistors [6] and spin Hall-effect applications [7]. The infinite spin lifetime in the PSH state is enforced by an SU(2) symmetry of the spin components, in which the effective field governing the spin precession of the itinerant electrons is momentum independent, thus robust to spin-independent disorder, including Coulomb and other many-body interactions [1]. Therefore, the spin scattering is essentially quenched in the PSH state, allowing precession in the same direction after a scattering event and potentially infinite spin lifetimes.

Although the PST is a highly sought spin texture for the aforementioned reasons, few materials with PSTs in the bulk are known [8]. Semiconducting GaAs/AlGaAs [2,9] and InGaAs/InAlAs [10,11] heterostructures can exhibit PSTs. In these artificial quasi–two-dimensional systems, PSTs arise from a balance between the strength of the Dresselhaus [12] and Rashba [13] spin splitting of the electronic bands. These effects are both correlated to the spin-orbital interaction (SOI) and require broken inversion symmetry [1,5,9–11]. Such a subtle balance can only be obtained by tuning the width of the quantum wells, electrostatic gating, and carrier concentration. If the interactions are not balanced, then the resulting effective momentum-dependent field removes the SU(2) symmetry and would permit scattering effects to reduce the spin lifetime through Dyakonov-Perel spin relaxation at low temperatures [6]. Therefore, these artificial structures require atomic precision during growth and carefully controlled carrier densities.

Recently, another mechanism for PSTs was proposed [14–29], which although remains to be confirmed experimentally [30], permits bulk materials to exhibit the spin texture without requiring the balancing of Dresselhaus and Rashba interactions through interface design. This symmetry-protected PST was predicted to occur when a nonsymmorphic symmetry operation (e.g., glide operation composed of a mirror plane and translation) commutes with the effective SOI field, $\boldsymbol{B}(\boldsymbol{k})$, in a material without inversion symmetry [16]; however, as we demonstrated recently [31], this is a sufficient but not necessary condition. These minimal ingredients enable a *unidirectional* spin orientation at the band edges in the electronic structure (spin-momentum locking), which in the absence of SOI would exist as a Kramers degeneracy. We also demonstrated that any noncentrosymmetric material with a high-symmetry k point exhibiting C_{2v} little-group symmetry with an even number of mirror operations intersecting at that position in the Brillouin zone can be a potential PST material [31]. This understanding can guide identification of crystals exhibiting PSTs in other achiral polar groups. This finding should allow us to surpass the apparent limitation of PSTs appearing as recent serendipitous discoveries in monoclinic and orthorhombic crystal systems [20]. Indeed, high-quality PST materials in the monoclinic crystal system are still missing, and surprisingly, there are no reported PST materials among the ferroelectric trigonal crystal system. Therefore, apart from the previous significant efforts in exploring PSTs in space groups with an even number of mirror symmetries, finding more materials and crystal classes with an odd number of mirror symmetries (i.e., monoclinic and trigonal crystal systems) showing PST would further enable experimental demonstration.

*jrondinelli@northwestern.edu

Here we use $\boldsymbol{k}\cdot\boldsymbol{p}$ models and first-principles calculations to show that PSTs can exist in polar structures of the trigonal crystal system. The PST is confined either along k paths with (symmetry protection) or without (symmetry unconstrained) mirror elements. Our main finding from our $\boldsymbol{k}\cdot\boldsymbol{p}$ model is that PSTs occur at the conduction band edge, if the conduction-band minimum appears near the midway point of the k path across the high-symmetry k point with C_s symmetry (with one mirror operation, m) in the trigonal noncentrosymmetric crystal classes. We predict Tl_3SbS_3 and $LiNbO_3$ satisfy this requirement and exhibit PSTs. Furthermore, thin-film versions of these two compounds subjected to coherent epitaxial constraints undergo a symmetry reduction from the C_{3v} crystal class with three mirror operations to C_s. The PSTs persist in thin films of these materials and their quality is enhanced, which we quantify using multiple criteria. The monoclinic Cm structure of Tl_3SbS_3 thin films supports a nearly perfect PST without any spin deviation that also simultaneously spans a large area of the Brillouin zone. These features enable access to the PST through chemical doping. Our study provides a promising route to find the persistent spin helix in 3D polar phases with long spin lifetimes.

II. COMPUTATIONAL METHODS

Our total energy calculations were based on density-functional theory (DFT) within the generalized gradient approximation utilizing the revised Perdew-Burke-Ernzerhof functional for solids [32] implemented in the Vienna *Ab initio* Simulation Package (VASP) [33–35]. We used a 550-eV plane-wave cutoff energy for all calculations and the projector augmented-wave method [36] with Li 1s and 2s electrons, Rb 4s, 4p, and 5s electrons, Tl 5d, 6s, and 6p electrons, Nb 4p, 4d, and 5s electrons, Ta 5p, 5d, and 6s electrons, Sb 5s and 5p electrons, O 2s and 2p electrons, and S 3s and 3p electrons treated as valence states. Gaussian smearing (0.10-eV width) is used for the Brillouin-zone integrations. The k-point sampling was tested and converged for the different cells. The convergence thresholds for the electronic relaxation and structure relaxation are 10^{-7} eV and 5 meV/Å, respectively. We tested the effects of SOI in the relaxation and found only tiny changes to the atomic structure; therefore, SOI effects were not included in structure relaxations.

III. RESULTS AND DISCUSSION

A. Identification of PST in the trigonal system

We consider trigonal systems, because they host common polar phases [23,37,38], such as in multiferroic $BiFeO_3$ [39] and polar chalcogenides Ag_3AsS_3 [40] with $R3c$ symmetries. Furthermore, a recent report showed a rational way to discover materials with strong Rashba coefficients, where commonly identified materials with large Rashba coefficients were found to exhibit space groups in trigonal and hexagonal crystal systems and corresponding C_{3v} or C_{6v} point groups (i.e., 20 out of 34 space groups) [41]. This contrasts with 6 out of 34 space groups found in monoclinic and orthorhombic crystal systems having C_{2v} or C_s point groups. Therefore, it is important to formulate a strategy to search and sort which compounds in the trigonal crystal system will exhibit PSTs to enable their discovery.

The symmetry operations of the $R3c$ phase with C_{3v} point group in Supplemental Material, Table 1 (Ref. [42]) allow us to deduce that there may be three unidirectional spin directions for the PST, which are along the [110], [100], and [010] directions of the hexagonal cell. The corresponding k paths for the [110], [100], and [010] directions are $\{[k,-k,k_z],[1/2,1/2,k_z],[-1/2,-1/2,k_z]\}$, $\{[k,-2k,k_z],[\mu,0,k_z]\}$, and $\{[2k,-k,k_z],\ [0,\nu,k_z]\}$, respectively, where μ and ν can take values of $\pm 1/2$. If we further constrain our investigation to the k_x-k_y plane, which will help keep the SU(2) symmetry and long spin lifetime under minimization of the commutator relations in Ref. [31], we find that the k paths for the [110], [100], and [010] unidirectional spin directions are $[k,-k,0]$, $[k,-2k,0]$, and $[2k,-k,0]$, respectively. Next, we assess whether symmetry requires the electronic bands to remain degenerate along these k paths. For the $[k,-k,0]$, $[k,-2k,0]$, and $[2k,-k,0]$ paths, the little-group symmetries of $\boldsymbol{k}$ are m^r_{110}, m^r_{100} and m^r_{010}, respectively. Because there is no $\mathcal{TG}$ in the little group leading to $(\mathcal{TG})^2\,\psi=-\psi$, there is no space-group symmetry protecting the Kramers degeneracy of the band edges by SOC effects for the three paths; therefore, the bands no longer touch along band trajectories in the k_x-k_y plane.

Next, we derive $\boldsymbol{k}\cdot\boldsymbol{p}$ models for each C_{3v} and C_s symmetry, because a k path with the mirror symmetry in the trigonal system, such as one of $[k,-k,0]$, $[k,-2k,0]$, and $[2k,-k,0]$, will connect the C_{3v} and C_s k points that we use to represent, for example, the zone center, Γ, and the zone boundary, Y, respectively. The detailed derivations of the $\boldsymbol{k}\cdot\boldsymbol{p}$ models are provided in Supplemental Material, Note 1 and Supplemental Tables 2–10 found in Ref. [42] (see also Refs. [43–49] therein). The $\boldsymbol{k}\cdot\boldsymbol{p}$ model with C_{3v} symmetry, spin-orbital coupling terms up to third order in k, and constrained in the k_x-k_y plane, is

$$\begin{aligned}\mathcal{H}_\Gamma &= \alpha_1 k_x\sigma_y+\alpha_2 k_y\sigma_x+\alpha_3 k_x\sigma_x+\alpha_4 k_y\sigma_y\\ &\quad+\beta_1\left(k_x^3-3k_xk_y^2\right)\sigma_z+\beta_2\left(k_x^3+k_xk_y^2\right)\sigma_y\\ &\quad+\beta_3\left(k_y^3+k_yk_x^2\right)\sigma_x+\beta_4\left(k_x^3+k_xk_y^2\right)\sigma_x\\ &\quad+\beta_5\left(k_y^3+k_yk_x^2\right)\sigma_y. \qquad (1)\end{aligned}$$

The same constraints applied to C_s symmetry give

$$\mathcal{H}_Y=\gamma_1 k_y\sigma_x+k_x(\gamma_2\sigma_y+\gamma_3\sigma_z), \qquad (2)$$

where α, β, and γ are the spin-orbital coupling coefficients, using a Cartesian coordinate system. The matrix forms for the wave functions including the spins for $\mathcal{H}_\Gamma$ and $\mathcal{H}_Y$ are

$$\psi_\Gamma=\begin{pmatrix}\bar{E}^2\\ \bar{E}^1\\ \bar{E}_1^1\\ \bar{E}_1^2\end{pmatrix}\quad\text{and}\ \psi_Y=\begin{pmatrix}\bar{E}^2\\ \bar{E}^1\end{pmatrix}, \qquad (3)$$

where $\bar{E}^2$, $\bar{E}^1$, and $\bar{E}_1$ in ψ_Γ are irreducible representations (*irreps*) of the double point group $3m$ (Supplemental Material, Note 1) [42]. $\bar{E}_1^1$ and $\bar{E}_1^2$ are the two components of the two-dimensional *irrep* $\bar{E}_1$. $\bar{E}^2$ and $\bar{E}^1$ in ψ_Y are *irreps* of the double point group m. Here, we only consider the symmetries of the

wave functions and not their exact forms. ψ_Γ transforms as a $D^{3/2}$ representation and $\binom{\bar{E}^2}{\bar{E}^1}$ transforms as a $D^{1/2}$ representation. With the Clebsch-Gordan (CG) coefficients, we can have the following for ψ_Γ:

$$\begin{aligned}\bar{E}^2 &= \eta_1^1 A_1 \bar{E}^2 + \eta_2^1 E^1 \bar{E}_1^2 + \eta_3^1 E^2 \bar{E}_1^1,\\ \bar{E}^1 &= -\eta_1^1 A_1 \bar{E}^1 + \eta_2^1 E^1 \bar{E}_1^2 + \eta_3^1 E^2 \bar{E}_1^1,\\ \bar{E}_1^1 &= \eta_1^2 E^2 \bar{E}_1^2,\\ \bar{E}_1^2 &= \eta_2^2 E^1 \bar{E}_1^1,\end{aligned} \tag{4}$$

where A_1 and E are the *irreps* of the double point group $3m$. E^1 and E^2 are the two components of the two-dimensional *irrep* E. Similarly, we obtain for ψ_Y

$$\begin{aligned}\bar{E}^2 &= \eta_1^3 A_1 \bar{E}^1 + \eta_2^3 A_2 \bar{E}_1^2,\\ \bar{E}^1 &= -\eta_1^3 A_1 \bar{E}^2 + \eta_3^3 A_2 \bar{E}_1^1,\end{aligned} \tag{5}$$

where A_1 and A_2 are the *irreps* of the double point group m, and η is a constant.

The above results can be applied to any space group with C_{3v} point symmetry. Through a detailed analysis of the polar structures of the trigonal system, we notice that there are two different trigonal polar space groups with the symmetries, that is,

Set 1: $P3m1$, $P31m$, $R3m$

Set 2: $P3c1$, $P31c$, $R3c$

In set 1, there are no glide (translation plus mirror) operations in the primitive cell. In set 2, there are nonsymmorphic (glide) symmetries. After we obtain the symmetries of the wave functions about the Γ point, it can be seen that in both wave functions represented by *irreps* $\bar{E}^2$ and $\bar{E}^1$, the d orbitals can be occupied by $\frac{1}{2}$-spin up (i.e., $\bar{E}_1^2$) and $\frac{1}{2}$-spin down (i.e., $\bar{E}_1^1$) at the same time. Furthermore, there is no symmetry constraint on making the spin-dependent d orbitals occupancies of E^1 (occupied by $\frac{1}{2}$-spin up) equal to E^2 (occupied by $\frac{1}{2}$-spin down). Therefore, if $k_y\sigma_y$ exists, such as along the k_y path with mirror symmetry, then σ_y cannot be canceled by any of the d orbitals of the same atom. Moreover, it is known that the spin in the k_y path will be constrained to be along the k_x direction by the mirror operation. So, σ_y is either canceled between two different atoms or there is no orbital having spin along σ_y. There are two atoms that can be connected by the mirror symmetry in $R3c$; therefore, if no σ_y occurs along the k_y path, there will remain orbitals having spins along σ_y at each atom leading to a reduction of spin magnitude along σ_x (i.e., the PST direction). In $R3m$, the mirror symmetry will transform one atom to itself, which will result in a situation in which there is no orbital having spin along σ_y. Thus, if there are PSTs in both $R3c$ and $R3m$, the quality of the PST as determined by the symmorphic mirror symmetry in $R3m$ should be better than that in $R3c$. Regarding the Y point, there is no σ_y allowed in the k_y path as indicated in Eq. (2); therefore, there is no significant reduction of the spin magnitude along σ_x in $R3c$.

Next, we derive whether PSTs exists in the $R3c$ and $R3m$ space groups. From Eqs. (1) and (2), we can see the spin direction will be uniform, that is, along the σ_x direction in the k_y path, regardless of the high-symmetry point considered. This is the same result as that in C_{2v}, because of the mirror symmetry in the k_y path. The main difference between C_{3v} and C_{2v} is that the spin deviation part led by k_x, which is present in the Hamiltonian having C_{2v} symmetry and contributes to the term $k_x\sigma_y$ about both Γ and Y, adds additional terms of the form $\beta_1(k_x^3 - 3k_xk_y^2)\sigma_z + \beta_2(k_x^3 + k_xk_y^2)\sigma_y + \beta_5 k_y k_x^2 \sigma_y$ around Γ and $\gamma_3 k_x \sigma_z$ around Y in C_{3v}. These terms are responsible for the spin deviation. From Eqs. (1) and (2), the spin-deviation angles (θ_y, θ_z) about Γ and Y with respect to σ_x are $[\arctan(\frac{k_x(\alpha_1+\beta_2 k_y^2)}{k_y(\alpha_2+\beta_3 k_y^2)+k_x(\alpha_3+\beta_4 k_y^2)}), \arctan(\frac{-3\beta_1 k_x k_y^2}{k_y(\alpha_2+\beta_3 k_y^2)+k_x(\alpha_3+\beta_4 k_y^2)})]$, and $[\arctan(\frac{\gamma_2 k_x}{\gamma_1 k_y}), \arctan(\frac{\gamma_3 k_x}{\gamma_1 k_y})]$, respectively. Then, a small deviation is expected to occur somewhere along the k_y path away from both the Γ and Y points, i.e., around the midway point of the k_y path, because large k_y minimizes the spin-deviation angles (θ_y, θ_z). This conclusion is also consistent with the results derived by solving Eq. (2) (see Supplemental Note 1, Eqs. S6–S11). Last, if the SOC parameters in the directions of σ_y and σ_z are also small, the angles (θ_y, θ_z) would further decrease. If the third-order terms are ignored in Eq. (1), we can obtain spin-deviation angles that reduce to $[\arctan(\frac{\alpha_1 k_x}{\alpha_2 k_y + \alpha_3 k_x}), 0]$, which is similar to the spin deviation present in the C_{2v} Hamiltonian. The PST phenomena were reported previously for materials with C_{2v} and C_s point groups. Here, the k_y path having the mirror symmetry in the C_{3v} point group resembles the points having C_{2v} symmetry and point having C_s symmetry. This simplification can be more effective when the k point is around the midway point of the k_y path, where the spin-deviation angles (θ_y, θ_z) are also minimal.

D. Validation of the $\boldsymbol{k} \cdot \boldsymbol{p}$ model

We now apply these guidelines to materials with C_{3v} point-group symmetry and compute the spin textures using density-functional theory calculations. We first choose $RbNbO_3$ with $R3m$ symmetry and $LiTaO_3$ with $R3c$ symmetry, whose primitive structures in real and reciprocal space are shown in Figs. 1(a), 1(b), 2(a), and 2(b). Both compounds are insulators and have a conduction-band minimum (CBM) at Γ [Figs. 1(c) and 2(c)]. The conduction band edges of both compounds indicate the PSTs occur along the k_x direction [Figs. 1(d) and 2(d)], because there is a mirror symmetry in the k_y path. The length of the arrows for the spin textures in Figs. 1(d) and 2(d) indicate that the spin amplitude along the k_x direction in $RbNbO_3$ is larger than that in $LiTaO_3$. This result is consistent with our $\boldsymbol{k} \cdot \boldsymbol{p}$ model, which finds that the spins along the k_y direction on the two Ta atoms with opposite directions are allowed and reduce the spins magnitude along the k_x direction (i.e., PST direction), when closer to the Γ point. Another conclusion from our $\boldsymbol{k} \cdot \boldsymbol{p}$ model analysis is that the PST can also occur at the midway point of the k_y path from Γ to Y as shown in Figs. 1(d) and 2(d). The PST areas with deviation angles $(5^\circ, 5^\circ)$ for the two materials are enclosed by the orange lines. If we want to access the PST and its associated helix experimentally, one additional requirement must be satisfied. The PST region should be located around the CBM to enable its access through n-type doping. Although we find the PST in both $RbNbO_3$ and $LiTaO_3$ materials, this requirement is not satisfied. The PSTs will be difficult to

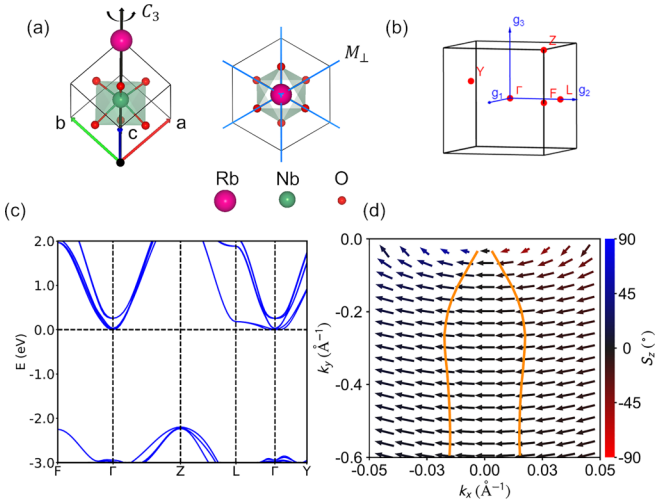

FIG. 1. (a) Trigonal cell of $RbNbO_3$ with $R3m$ symmetry along the threefold axis. The mirror symmetries are also shown. (b) Brillouin zone of the trigonal-cell reciprocal lattice vectors (g_1, g_2, g_3). High-symmetry k points are shown in red with values specified in Supplemental Material, Table 11 [42]. (c) Band structure of the trigonal cell. The energy is given with respect to the CBM. (d) Spin textures in the $k_z = 0$ (fractional coordinate) plane of the lowest conduction band around the $\Gamma - Y$ path. Arrows indicate the spin direction. Color scale represents the degree of spin deviation out of the xy plane (i.e., along the k_z direction). Area within the orange lines indicates spin deviations less than (5°, 5°).

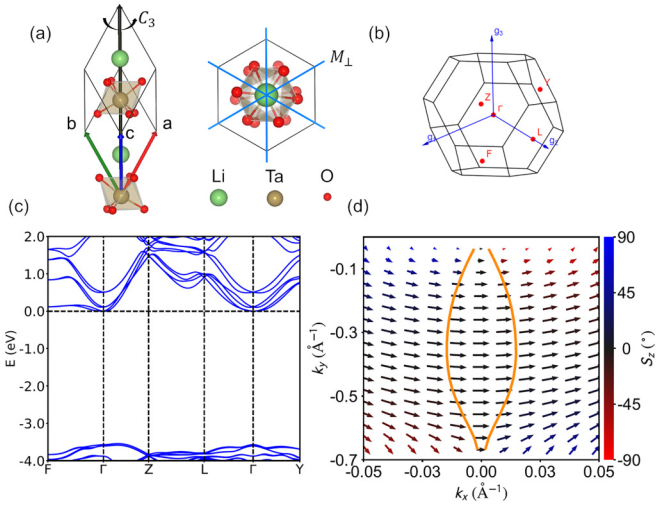

FIG. 2. (a) Trigonal cell of $LiTaO_3$ with $R3c$ symmetry along the threefold axis. Mirror symmetries are also shown. (b) Brillouin zone of the trigonal cell with reciprocal lattice vectors (g_1, g_2, g_3). High-symmetry k points are shown in red with values specified in Supplemental Material, Table 11 [42]. (c) Band structure of the trigonal cell. Energy is given with respect to the CBM. (d) Spin textures in the $k_z = 0$ (fractional coordinate) plane of the lowest conduction band around the $\Gamma - Y$ path. Arrows indicate the spin direction. Color scale represents the degree of spin deviation out of the xy plane (i.e., along the k_z direction). Area within the orange lines indicates spin deviations less than (5°, 5°).

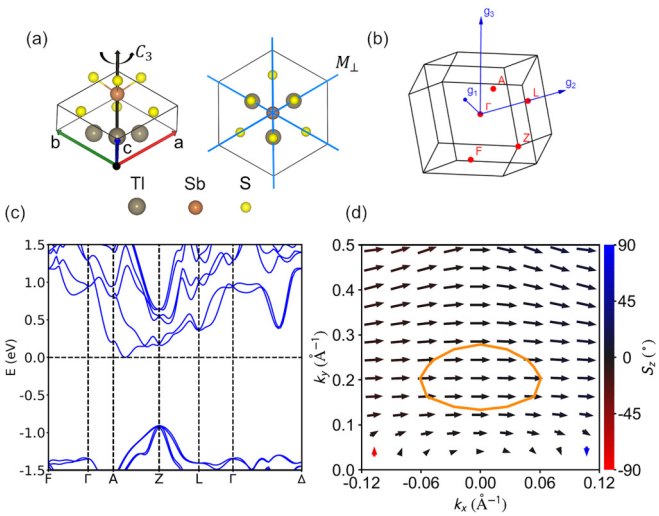

FIG. 3. (a) Trigonal cell of Tl_3SbS_3 with $R3m$ symmetry along the threefold axis. Mirror symmetries are also shown. (b) Brillouin zone of the trigonal cell with reciprocal lattice vectors (g_1, g_2, g_3). High-symmetry k points are shown in red and specified in Supplemental Material, Table 12 [42]. (c) Band structure of the trigonal cell. Energy is given with respect to the CBM. (d) Spin textures in the $k_z = 1/2$ (fractional coordinate) plane of the lowest conduction band around the $A - Z$ path. Arrows indicate the spin direction. Color scale represents the degree of spin deviation out of the xy plane (i.e., along the k_z direction). Area within the orange lines indicates spin deviations less than (5°, 5°).

access because the PST region is at a much higher energy than the CBM.

E. Identification of PSTs in Tl_3SbS_3 and $LiNbO_3$

We now apply our group theory analysis and $\boldsymbol{k} \cdot \boldsymbol{p}$ model to Tl_3SbS_3 with a polar $R3m$ ground-state structure [50] [Figs. 3(a) and 3(b)]. Our computed electric polarization is approximately 23 μC cm^{-2}. The band structure of Tl_3SbS_3 reveals it has a DFT indirect band gap of 0.88 eV in bulk with the CBM along the $A' - Z$ path [Fig. 3(c)]. We find $A' - Z$: (1/6,1/6,1/6)→(1/2,1/2, −1/2) at a $k_z = \frac{1}{2}$ (fractional coordinate) plane [Fig. 3(c)], which exhibits a mirror symmetry perpendicular to x, can be transformed to a $[k, -k, 1/2]$ path in a hexagonal system. Following the group analysis above, the unidirectional spin direction should then be along the x direction since the mirror symmetry is perpendicular to x. Indeed, Fig. 3(d) shows there is a PST with a unidirectional spin direction along the x direction for bands dispersing along the k_y direction. Since the PST region is at a $k_z = \frac{1}{2}$ plane, the spin deviation is unaffected by k_z. Because space group $R3m$ has threefold rotational symmetry, we expect three directions in the Brillouin zone exhibit a PST, which are symmetry related to each other, and provide persistent spin helices.

To determine the spin lifetime for the PSHs in Tl_3SbS_3, we adopt a Hamiltonian with C_s symmetry, because the PST region is located around the middle of the k_y path with a mirror operation. The SOC strength in the PST region along k_y are $\gamma_1 = 0.69$ eVÅ and those along k_x are $\gamma_2 = 0.06$ eVÅ and $\gamma_3 = 0.71$ eVÅ. Figure 3(d) shows that the PST persists and

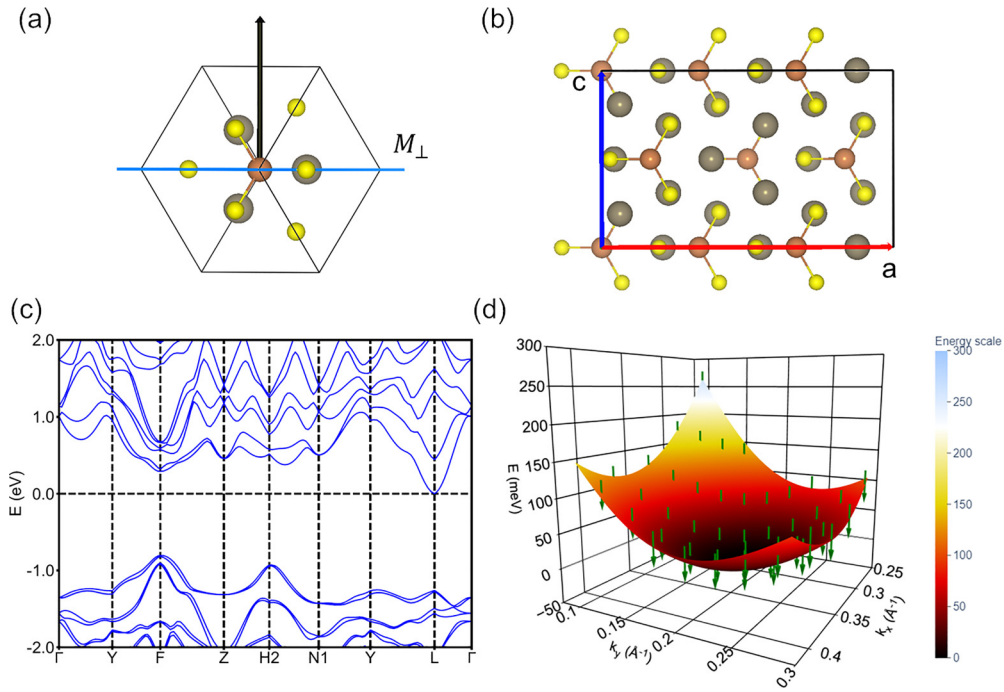

FIG. 4. (a) Orientation for building thin films from Tl_3SbS_3 with a trigonal cell and $R3m$ symmetry. Black arrow indicates the film direction. (b) Structure of Tl_3SbS_3 film with Cm symmetry. Brillouin zone of the film is the same as that of the trigonal cell. Values of the high-symmetry k points are specified in Supplemental Material, Table 13 [42]. (c) Band structure of the film. Energy is given with respect to the CBM. (d) Energy surface of the lowest conduction band spanning a $k_x - k_y$ plane around the $\Gamma - L$ path. Arrows indicate the spin direction. Color scale represents the band energies. All the spins are oriented along the k_z direction.

spans an area from the CBM to 45 meV above it. Simultaneously, the spin deviation away from the x direction is also less than $(5^\circ, 5^\circ)$. With the SOC parameters and a Fermi wavelength $k_F = 0.025\,\text{Å}^{-1}$, we compute the spin lifetime $\tau_s \cong 1$ ps for the PSH mode and the characteristic spin lifetime is $\frac{\tau_s}{T_{PSH}} = 8.8$, where the spin-procession period time $T_{PSH} = \frac{\pi\hbar}{\gamma_1 k_F}$. The spin lifetime in Tl_3SbS_3 is much shorter compared to canonical materials such as GaAs/AlGaAs (∼200) [45].

To further enhance the quality of the PST in Tl_3SbS_3, we need to eliminate the influence of the SOC terms along k_x. Often when investigating Rashba, Dresselhaus, and persistent spin textures in quantum-well materials, $\boldsymbol{k}\cdot\boldsymbol{p}$ models in two dimensions are invoked and the average momentum along the *out-of-plane* direction of a confined electron gas or thin-film/heterostructure is set to zero within a mean-field approximation. The consequence is that odd-order SOC terms in the Hamiltonian can be neglected. In a similar way, we build a thin film with k_x along the out-of-plane direction and a mirror symmetry in the *in-plane* direction. Since k_y and k_z then become the in-plane reciprocal lattice vectors for the thin film, we explore the SOC terms along both k_y and k_z directions. Based on C_s symmetry, we have $\gamma_1' k_z \sigma_x$ in $\mathcal{H}_Y$, which also supports the uniform spin direction along the k_x direction same as that led by the SOC effects along the k_y direction [Eq. (2)]. Therefore, a thin film on (011) $TbAlO_3$ substrate with its out-of-plane (in-plane) direction aligned along k_x (k_y and k_z) of the bulk structure [see Figs. 4(a) and 4(b)] should support a uniform spin direction along the out-of-plane direction with zero spin deviation. This behavior is demonstrated by our direct DFT calculations [Fig. 4(d)] with strains along the a and b directions of 1.8 and −0.2%, respectively. We find a perfect PST spanning a large portion of the Brillouin zone and a high-energy range above the CBM.

If we further redefine the in-plane direction (k_x') of the thin film to be along $\gamma_1 k_y + \gamma_1' k_z$ of the bulk state, which is a direction about 34° away from k_z direction, then the CBM occurs along this direction in the thin film as seen in the $\Gamma - L$ path of the band structure [Fig. 4(c)]. The SOC parameter is 1.71 eVÅ around the CBM along the $\Gamma - L$ path, which is comparable to other predicted PST materials with strong SOC coefficients, such as that of 1.9 eVÅ in $BiInO_3$. The Tl_3SbS_3 film is a three-dimensional material showing a perfect PST without any spin deviation. Our finding stems from careful analyses of trigonal polar groups and reducing the C_{3v} crystal class to C_s by engineering an epitaxial thin film using demonstrated approaches [39] applied to realize monoclinic $BiFeO_3$. Figure 4(b) shows that a Tl_3SbS_3 film has Cm symmetry and the computed polarization for this phase is about 23 μC cm^{-2} along the b direction. Because there is no spin deviation, the spin lifetime will ideally diverge toward infinity at low temperatures until another spin-scattering mechanism becomes operative. Alternative to the thin-film geometry [51], this optimal PST may also be observed in bulk Tl_3SbS_3 along the k_x direction via laser-induced formation of surface nanolayers [52].

A PSH state with the spin-spiral plane perpendicular to the unidirectional effective field has long been pursued [5].

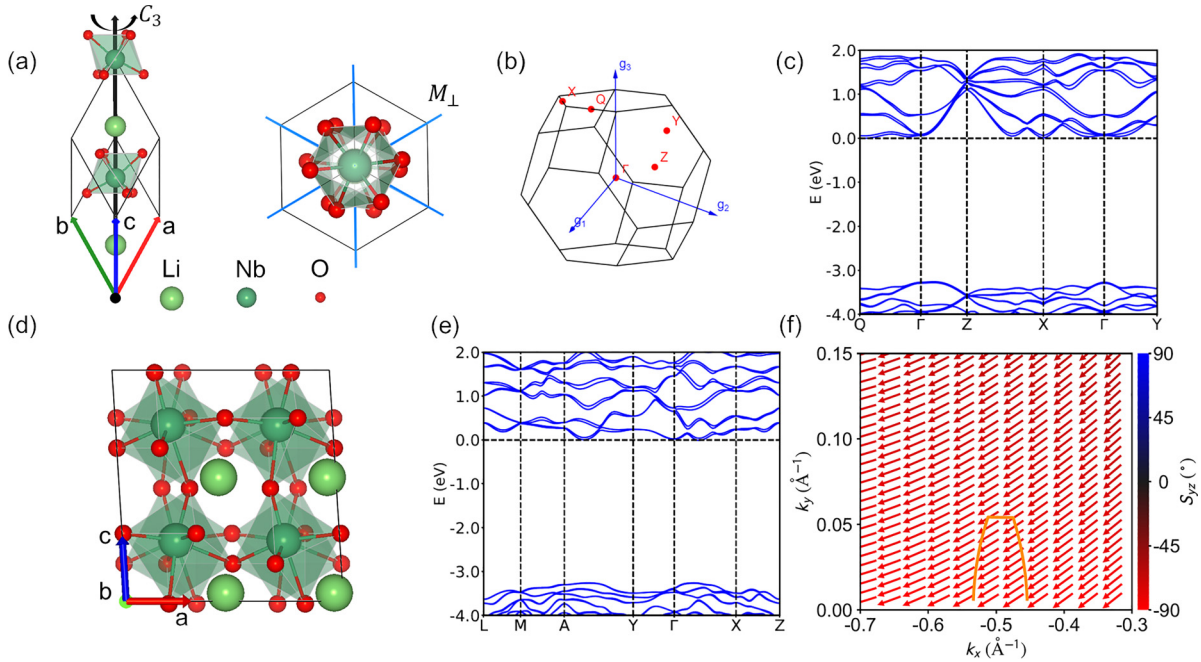

FIG. 5. (a) Trigonal cell of $LiNbO_3$ with $R3c$ symmetry along the threefold axis. Mirror symmetries are also shown. (b) Brillouin zone of the trigonal cell with reciprocal lattice vectors (g_1, g_2, g_3). High-symmetry k points are shown in red with values specified in Supplemental Material, Table 14 [42]. (c) Band structure of the trigonal cell. Energy is given with respect to the CBM. (d) Structure of a $LiNbO_3$ film with Cc symmetry. Brillouin zone of the film is the same as that of the trigonal cell. Values of the high-symmetry k points are shown in Supplemental Material, Table 15 [42]. (e) Band structure of the film. (f) Spin textures in the $k_z = 0$ (fractional coordinate) plane of the lowest conduction band around the $\Gamma - Y$ path. Arrow indicates the spin direction. Color scale represents the degree of spin deviation out of the xy plane (i.e., along the k_z direction). Area within the orange lines indicates spin deviations less than (5°, 5°). Arrow indicates the spin direction (in the yz plane) projected into the $k_z = 0$ plane, whose components along k_x and k_y in the plot are along the Cartesian y and z directions, respectively. Color scale represents the degree of spin deviation out of the yz plane (i.e., along the k_x direction), that is, 90° indicates the spin is in the yz plane. Area within the orange lines indicates spin deviation towards the k_x direction is less than 10°.

By solving a microscopic spin-diffusion equation in quantum-well structures, previous studies found an enhanced spin lifetime τ_s occurs at a "magic" wave vector of $2q$, where q corresponds to the shifting vector induced by the Kramers degeneracy from time-reversal symmetry on the Fermi surface [1,5]. This well-known PSH state at $2q$ occurs as a consequence of the C_{2v} or C_s symmetry of the SOC Hamiltonian—the only two previously known symmetries of the SOC Hamiltonian that can produce the PSH state with a long spin lifetime [5,20]. This PSH mode is due to a PST spin texture that occurs in a $\boldsymbol{k}$ path starting from a high-symmetry k point having C_{2v} or C_s symmetry, resulting in a uniform spin direction that is in a direction perpendicular to the $\boldsymbol{k}$ path [31]. However, there exists a $\boldsymbol{k}$ path under C_s symmetry, which may induce a spin texture: $k_x(\gamma_2\sigma_y + \gamma_3\sigma_z)$ such that k_x does not contain a mirror plane. In this defined spin texture, the spin texture in the plane perpendicular to k_x depends on the ratio of γ_2/γ_3. This special situation can occur because the SOC strengths along k_y are smaller than those along the k_x direction. Therefore, we call the PST along a k path without mirror symmetry a type-II or accidental PST to contrast it with type-I PSTs that are enforced along a k path with a mirror symmetry.

Next, we will elucidate how a type-II PST occurs in the important optoelectronic material $LiNbO_3$ [53] [Fig. 5(a)], for which we calculate an electric polarization of 68 μC cm^{-2}. Our computed polarization is underestimated compared with the experimentally observed polarization [54] (77 μC cm^{-2}). Figure 5(c) shows that the CBM is not along a high-symmetry k_y path having the mirror symmetry but is at different k point compared to $LiTaO_3$ where the CBM is in the k_y path. The location of the CBM in $LiNbO_3$ is consistent with the previous calculations [55]. Since we are interested in the $k_x - k_y$ plane for searching for possible PST regions, we construct a thin-film $LiNbO_3$ geometry with Cc symmetry ($a \approx b = 3.68$ Å) [see Fig. 5(d)], which should be accessible in experiment using demonstrated growth approaches [39] to realize Cc $BiFeO_3$. The computed polarization for the film is 71 μC cm^{-2} along a direction 37° from the c direction in the (110) plane. We find that the CBM is located at a point in the k_x path along the [110] direction in the thin film. We further interpolate the band structure in a $k_x - k_y$ plane at $k_z = 0$ by carrying out WANNIER90+SOC calculations (Supplemental Material, Fig. 1) [42], which further supports our identification of the CBM as the minimum energy along the k_x path. Surprisingly, although the k_x path only possesses the identify operation, there is still a region showing a uniform spin direction determined by $\gamma_2\sigma_y + \gamma_3\sigma_z$. This type-II PST region also has a sizable area as shown in Fig. 5(f), enclosed by the (orange) boundary line demarcating the spin deviation from a direction determined by $\gamma_2\sigma_y + \gamma_3\sigma_z$ [i.e., $\sim\arctan(\gamma_3/\gamma_2) = 33°$ from the k_y direction] is also less than 10°. The SOC strength in

the PST region along k_y is $\gamma_1 = 0.14$ eV Å and along k_x it is $\gamma_2 = 0.51$ eV Å and $\gamma_3 = 0.33$ eV Å in the Cc structure. With these SOC parameters and a Fermi wavelength of 0.04 Å^{-1}, we compute the spin lifetime for the PSH mode in $LiNbO_3$ to be 11 ps and $\frac{\tau_s}{\tau_{PSH}} = 127$. Therefore, a possibly better PST in the polar structure with C_{3v} symmetry can be obtained by reducing its symmetry to C_s in a thin film, while there is no PST accessible in bulk $R3c$ structure.

IV. CONCLUSION

We proposed a strategy to identify and design optimal PSTs in bulk crystals based on polar space groups showing an odd number of mirror operations. We showed that compounds with point groups C_{3v} may also exhibit PSTs, which expands the phenomenon to more readily n-type dopable chalcogenide compounds and perovskite oxides with $R3c$ and $R3m$ symmetries. We also found that using strain to reduce the crystalline symmetry is a useful strategy for improving the performance of bulk PST materials and unlocking hidden type-II (or accidental) PSTs in thin films of many previously identified Rashba compounds [23,50]. This approach brings PST properties to more complex crystal structures and chemistries with strong Rashba coefficients and/or topological insulator and Weyl semimetal phases. Noncentrosymmetric compounds with high-symmetry wave vectors in reciprocal space exhibiting C_s point symmetry are an important initial phase space to search for PSTs in known materials. Last, our study demonstrates a type of PST that does not require symmetry protection, which will bring further opportunities to find high-quality PSHs in future spin-orbitronic devices.

ACKNOWLEDGMENTS

X.-Z.L. and J.M.R. were supported by the National Science Foundation (NSF) under Grant No. DMR-2104397. DFT calculations were performed on the CARBON cluster at the Center for Nanoscale Materials at Argonne National Laboratory and the Extreme Science and Engineering Discovery Environment (XSEDE), which is supported by the NSF (Grant No. ACI-1548562). Use of the Center for Nanoscale Materials, an Office of Science user facility, was supported by the U.S. Department of Energy, Office of Science, Office of Basic Energy Sciences, under Contract No. DE-AC02-06CH11357.

[1] B. A. Bernevig, J. Orenstein, and S. C. Zhang, Exact SU(2) Symmetry and Persistent Spin Helix in a Spin-Orbit Coupled System, Phys. Rev. Lett. **97**, 236601 (2006).
[2] J. D. Koralek, C. P. Weber, J. Orenstein, B. A. Bernevig, S. C. Zhang, S. MacK, and D. D. Awschalom, Emergence of the persistent spin helix in semiconductor quantum wells, Nature (London) **458**, 610 (2009).
[3] J. Schliemann, J. C. Egues, and D. Loss, Nonballistic Spin-Field-Effect Transistor, Phys. Rev. Lett. **90**, 146801 (2003).
[4] A. Manchon, H. C. Koo, J. Nitta, S. M. Frolov, and R. A. Duine, New perspectives for Rashba spin-orbit coupling, Nat. Mater. **14**, 871 (2015).
[5] J. Schliemann, Colloquium: Persistent spin textures in semiconductor nanostructures, Rev. Mod. Phys. **89**, 011001 (2017).
[6] M. I. Dyakonov and V. I. Perel, Spin relaxation of conduction electrons in noncentrosymmetric semiconductors, Sov. Phys. Solid State **13**, 3023 (1972).
[7] S. Datta and B. Das, Electronic analog of the electro-optic modulator, Appl. Phys. Lett. **56**, 665 (1998).
[8] F. Dettwiler, J. Fu, S. Mack, P. J. Weigele, J. C. Egues, D. D. Awschalom, and D. M. Zumbühl, Stretchable Persistent Spin Helices in GaAs Quantum Wells, Phys. Rev. X **7**, 031010 (2017).
[9] M. P. Walser, C. Reichl, W. Wegscheider, and G. Salis, Direct mapping of the formation of a persistent spin helix, Nat. Phys. **8**, 757 (2012).
[10] M. Kohda *et al.*, Gate-controlled persistent spin helix state in (In,Ga)as quantum wells, Phys. Rev. B **86**, 081306(R) (2012).
[11] A. Sasaki, S. Nonaka, Y. Kunihashi, M. Kohda, T. Bauernfeind, T. Dollinger, K. Richter, and J. Nitta, Direct determination of spin–orbit interaction coefficients and realization of the persistent spin helix symmetry, Nat. Nanotechnol. **9**, 703 (2014).
[12] G. Dresselhaus, Spin-orbit coupling effects in zinc blende structures, Phys. Rev. **100**, 580 (1955).
[13] E. I. Rashba, Semiconductors with a loop of extrema, J. Electr. Spectros. Relat. Phenom. **201**, 4 (2015).
[14] M. A. U. Absor, F. Ishii, H. Kotaka, and M. Saito, Persistent spin helix on a wurtzite ZnO(10$\bar{1}$0) surface: First-principles density-functional study, Appl. Phys. Express **8**, 073006 (2015).
[15] N. Yamaguchi and F. Ishii, Strain-induced large spin splitting and persistent spin helix at LaAlO3/SrTiO3 interface, Appl. Phys. Express **10**, 123003 (2017).
[16] L. L. Tao and E. Y. Tsymbal, Persistent spin texture enforced by symmetry, Nat. Commun. **9**, 2763 (2018).
[17] C. Autieri, P. Barone, J. Sławińska, and S. Picozzi, Persistent spin helix in Rashba-Dresselhaus ferroelectric $CsBiNb_2O_7$, Phys. Rev. Mater. **3**, 084416 (2019).
[18] H. Djani, A. C. Garcia-Castro, W. Y. Tong, P. Barone, E. Bousquet, S. Picozzi, and P. Ghosez, Rationalizing and engineering Rashba spin-splitting in ferroelectric oxides, npj Quantum Mater. **4**, 51 (2019).
[19] F. Jia, S. Hu, S. Xu, H. Gao, G. Zhao, P. Barone, A. Stroppa, and W. Ren, Persistent spin-texture and ferroelectric polarization in 2d hybrid perovskite benzylammonium lead-halide, J. Phys. Chem. Lett. **11**, 5177 (2020).
[20] Moh. Adhib Ulil Absor, I. Santoso, N. Yamaguchi, and F. Ishii, Spin splitting with persistent spin textures induced by the line defect in the 1t phase of monolayer transition metal dichalcogenides, Phys. Rev. B **101**, 155410 (2020).
[21] X. Li, S. Zhang, H. Huang, L. Hu, F. Liu, and Q. Wang, Unidirectional spin-orbit interaction induced by the line defect in monolayer transition metal dichalcogenides for high-performance devices, Nano Lett. **19**, 6005 (2019).
[22] H. Lee, J. Im, and H. Jin, Emergence of the giant out-of-plane Rashba effect and tunable nanoscale persistent spin helix in ferroelectric SnTe thin films, Appl. Phys. Lett. **116**, 022411 (2020).

[23] L. G. Davanse da Silveira, P. Barone, and S. Picozzi, Rashba-Dresselhaus spin-splitting in the bulk ferroelectric oxide BiAlO3, Phys. Rev. B **93**, 245159 (2016).

[24] L. L. Tao and E. Y. Tsymbal, Perspectives of spin-textured ferroelectrics, J. Phys. D: Appl. Phys. **54**, 113001 (2021).

[25] M. Adhib Ulil Absor, A. Lukmantoro, and I. Santoso, Full-zone persistent spin textures with giant spin splitting in two-dimensional group IV-V compounds, J. Phys.: Condens. Matter **34**, 445501 (2022).

[26] N. Yang, G. Gou, X. Lu, and Y. Hao, Linear dichroism and polarization controllable persistent spin helix in two-dimensional ferroelectric $ZrOI_2$ monolayer, Nano Res. **15**, 6779 (2022).

[27] J. Ji, F. Lou, R. Yu, J. S. Feng, and H. J. Xiang, Symmetry-protected full-space persistent spin texture in two-dimensional materials, Phys. Rev. B **105**, L041404 (2022).

[28] H. J. Zhao, H. Nakamura, R. Arras, C. Paillard, P. Chen, J. Gosteau, X. Li, Y. Yang, and L. Bellaiche, Purely Cubic Spin Splittings with Persistent Spin Textures, Phys. Rev. Lett. **125**, 216405 (2020).

[29] L. Zhang, J. Jiang, C. Multunas, C. Ming, Z. Chen, Y. Hu, Z. Lu, S. Pendse, R. Jia, M. Chandra, Y.-Y. Sun, T.-M. Lu, Y. Ping, R. Sundararaman, and J. Shi, Room-temperature electrically switchable spin–valley coupling in a van der Waals ferroelectric halide perovskite with persistent spin helix, Nat. Photon. **16**, 529 (2022).

[30] M. Acharya, S. Mack, A. Fernandez, J. Kim, H. Wang, K. Eriguchi, D. Meyers, V. Gopalan, J. Neaton, and L. W. Martin, Searching for new ferroelectric materials using high-throughput databases: An experimental perspective on $BiAlO_3$ and $BiInO_3$, Chem. Mater. **32**, 7274 (2020).

[31] X. Z. Lu and J. M. Rondinelli, Discovery principles and materials for symmetry-protected persistent spin textures with long spin lifetimes, Matter **3**, 1211 (2020).

[32] J. P. Perdew, A. Ruzsinszky, G. I. Csonka, O. A. Vydrov, G. E. Scuseria, L. A. Constantin, X. Zhou, and K. Burke, Restoring the Density-Gradient Expansion for Exchange in Solids and Surfaces, Phys. Rev. Lett. **100**, 136406 (2008).

[33] G. Kresse and J. Furthmüller, Efficient iterative schemes for ab initio total-energy calculations using a plane-wave basis set, Phys. Rev. B **54**, 11169 (1996).

[34] G. Kresse and J. Furthmüller, Efficiency of ab-initio total energy calculations for metals and semiconductors using a plane-wave basis set, Comput. Mater. Sci. **6**, 15 (1996).

[35] G. Kresse and D. Joubert, From ultrasoft pseudopotentials to the projector augmented-wave method, Phys. Rev. B **59**, 1758 (1999).

[36] P. E. Blöchl, Projector augmented-wave method, Phys. Rev. B **50**, 17953 (1994).

[37] H. J. Zhao, P. Chen, C. Paillard, R. Arras, Y. W. Fang, X. Li, J. Gosteau, Y. Yang, and L. Bellaiche, Large spin splittings due to the orbital degree of freedom and spin textures in a ferroelectric nitride perovskite, Phys. Rev. B **102**, 041203(R) (2020).

[38] A. Fernandez, M. Acharya, H.-G. Lee, J. Schimpf, Y. Jiang, D. Lou, Z. Tian, and L. W. Martin, Thin-film ferroelectrics, Adv. Mater. **34**, 2108841 (2022).

[39] J. Wang *et al.*, Epitaxial $BiFeO_3$ multiferroic thin film heterostructures, Science **299**, 1719 (2003).

[40] M. G. Vergniory, L. Elcoro, C. Felser, N. Regnault, B. A. Bernevig, and Z. Wang, A complete catalogue of high-quality topological materials, Nature (London) **566**, 480 (2019).

[41] C. Mera Acosta, E. Ogoshi, A. Fazzio, G. M. Dalpian, and A. Zunger, The Rashba scale: Emergence of band anti-crossing as a design principle for materials with large Rashba coefficient, Matter **3**, 145 (2020).

[42] See Supplemental Material at http://link.aps.org/supplemental/10.1103/PhysRevB.xx.xxxxxx for $\boldsymbol{k}\cdot\boldsymbol{p}$ model, spin-diffusion equation, interpolated band structures of the *R3c* and *Cc* structures of $LiNbO_3$ from WANNIER90+SOC calculations, and additional data tables.

[43] J. Bardeen, An improved calculation of the energies of metallic Li and Na, J. Chem. Phys. **6**, 367 (2004).

[44] F. Seitz, *The Modern Theory of Solids*, 1st ed. (McGraw-Hill, New York, 1940).

[45] X. Liu and J. Sinova, Unified theory of spin dynamics in a two-dimensional electron gas with arbitrary spin-orbit coupling strength at finite temperature, Phys. Rev. B **86**, 174301 (2012).

[46] M. I. Aroyo, A. Kirov, C. Capillas, J. M. Perez-Mato, and H. Wondratschek, Bilbao crystallographic server. II. Representations of crystallographic point groups and space groups, Acta Cryst. **A62**, 115 (2006).

[47] M. I. Aroyo, J. M. Perez-Mato, D. Orobengoa, E. Tasci, G. de La Flor, and A. Kirov, Crystallography online: Bilbao crystallographic server, Bulg. Chem. Commun. **43**, 183 (2011).

[48] M. I. Aroyo, J. M. Perez-Mato, C. Capillas, E. Kroumova, S. Ivantchev, G. Madariaga, A. Kirov, and H. Wondratschek, Bilbao crystallographic server: I. databases and crystallographic computing programs, Z. Kristallogr. **221**, 15 (2006).

[49] G. Pizzi *et al.*, Wannier90 as a community code: New features and applications, J. Phys.: Condens. Matter **32**, 165902 (2020).

[50] A. Olsen, P. Goodman, and H. J. Whitfield, The structure Tl_3SbS_3, Tl_3SbSe_3, $Tl_3SbS_{3-x}Se_x$, and $Tl_3Sb_yAs_{1-y}Se_3$, J. Solid State Chem. **60**, 305 (1985).

[51] G. F. Harrington, A. Cavallaro, D. W. McComb, S. J. Skinner, and J. A. Kilner, The effects of lattice strain, dislocations, and microstructure on the transport properties of YSZ Films, Phys. Chem. Chem. Phys. **19**, 14319 (2017).

[52] K. Ozga, A. O. Fedorchuk, A. M. El-Naggar, A. A. Albassam, and V. Kityk, Formation of surface nanolayers in chalcogenide crystals using coherent laser beams, Physica E **97**, 302 (2018).

[53] M. Sumets, Lithium Niobate-Based Heterostructures: Synthesis, properties and electron phenomena: Thin films of lithium niobate: potential applications, synthesis methods, structure and properties (IOP Publishing Ltd, 2018), pp. 1-1–1-42.

[54] L. Hafid and F. M. Michel-Calendini, Electronic structure of LiNbO3: Densities of states, optical anisotropy and spontaneous polarisation calculated from the Xα molecular orbital method, J. Phys. C: Solid State Phys. **19**, 2907 (1986).

[55] A. Jain *et al.*, Commentary: The materials project: A materials genome approach to accelerating materials innovation, APL Mater. **1**, 011002 (2013).